

# CT-Mamba: A Hybrid Convolutional State Space Model for Low-Dose CT Denoising

Linxuan Li<sup>a</sup>, Wenjia Wei<sup>a</sup>, Luyao Yang<sup>a</sup>, Wenwen Zhang<sup>a</sup>, Jiashu Dong<sup>a,d</sup>, Yahua Liu<sup>b</sup>, Hongshi Huang<sup>c</sup>, Wei Zhao<sup>a,d,e,\*</sup>

<sup>a</sup>*School of Physics, Beihang University, Beijing, China*

<sup>b</sup>*Emergency Department of the Third Medical Center, Chinese PLA General Hospital, Beijing, China*

<sup>c</sup>*Department of Sports Medicine, Peking University Third Hospital, Institute of Sports Medicine of Peking University, Beijing Key Laboratory of Sports Injuries, Engineering Research Center of Sports Trauma Treatment Technology and Devices, Ministry of Education, Beijing, China*

<sup>d</sup>*Hangzhou International Innovation Institute, Beihang University, Hangzhou, China*

<sup>e</sup>*Tianmushan Laboratory, Hangzhou, China*

---

## Abstract

Low-dose CT (LDCT) significantly reduces the radiation dose received by patients, however, dose reduction introduces additional noise and artifacts. Currently, denoising methods based on convolutional neural networks (CNNs) face limitations in long-range modeling capabilities, while Transformer-based denoising methods, although capable of powerful long-range modeling, suffer from high computational complexity. Furthermore, the denoised images predicted by deep learning-based techniques inevitably exhibit differences in noise distribution compared to normal-dose CT (NDCT) images, which can also impact the final image quality and diagnostic outcomes. This paper proposes CT-Mamba, a hybrid convolutional State Space Model for LDCT image denoising. The model combines the local feature extraction advantages of CNNs with Mamba's strength in capturing long-range dependencies, enabling it to capture both local details and global context. Additionally, we introduce an innovative spatially coherent Z-shaped scanning scheme to ensure spatial continuity between adjacent pixels in the image. We design a Mamba-driven deep noise power spectrum (NPS) loss function to guide model training, ensuring that the noise texture of the denoised LDCT images closely resembles that of NDCT images, thereby enhancing overall image quality and diagnostic value. Experimental results have demonstrated that CT-Mamba performs excellently in reducing noise in LDCT images, enhancing detail preservation, and optimizing noise texture distribution, and exhibits higher statistical similarity with the radiomics features of NDCT images. The proposed CT-Mamba demonstrates outstanding performance in LDCT denoising and holds promise as a representative approach for applying the Mamba framework to LDCT denoising tasks.

*Keywords:* Low-Dose CT, Denoising, State Space Model, Mamba, Noise Power Spectrum

---

## 1. Introduction

Computed tomography (CT) is an essential imaging technique in clinical practice, providing crucial anatomical information that aids physicians in making appropriate medical decisions (Zhang et al.,

---

\*Corresponding author.

<sup>1</sup>Linxuan Li and Wenjia Wei contributed equally to this work.

<sup>2</sup><https://github.com/linxuan-li/CT-Mamba>

<sup>3</sup>Email: [linxuan.li@163.com](mailto:linxuan.li@163.com), [weiwenjia@buaa.edu.cn](mailto:weiwenjia@buaa.edu.cn)

<sup>4</sup>DOI: [10.1016/j.compmedimag.2025.102595](https://doi.org/10.1016/j.compmedimag.2025.102595)

2025; Lv et al., 2024). However, frequent CT scans can significantly increase the radiation dose received by patients, particularly in radiation therapy, where multiple scans are often required to achieve precise tumor localization and minimize damage to organs at risk. Excessive radiation may harm the patient, impact organ function, increase the incidence of radiation-related diseases linked to genetic damage, and ultimately reduce the patient's quality of life. Therefore, reducing the radiation dose of CT imaging has become a focus of attention. Low-dose CT (LDCT) is an effective method for reducing patient radiation exposure (Bosch de Basea Gomez et al., 2023). In clinical practice, to acquire LDCT images, it is common to reduce the tube current to decrease the flux of the electron beam that generates X-ray photons, and/or reduce the number of projections during CT procedures. While these methods reduce radiation dose, they also introduce additional noise and artifacts, which decrease the overall quality of the image. If these issues are not effectively addressed, they will significantly impact the application of LDCT in various clinical scenarios. How to obtain high-quality CT images that are comparable to normal-dose CT (NDCT) images and meet the clinical utilities from low-dose scanning protocols has become a long-standing and practically significant problem in the field of CT imaging.

To address this issue, several LDCT imaging algorithms have been proposed, which can be roughly divided into the following three categories (Zhang et al., 2024a; Li et al., 2025b; Zhang et al., 2021): sinogram-based preprocessing, iterative reconstruction, and image post-processing. Sinogram-based preprocessing methods directly target the raw data acquisition stage and designs specific filters for processing CT projection data obtained through low-dose X-rays. Typical methods include bilateral filtering (Manduca et al., 2009), structure-adaptive filtering (Balda et al., 2012), and penalized weighted least squares (Wang et al., 2006). These denoising methods combine physical characteristics with photon statistical characteristics, making them relatively simple and easy to implement. However, these methods rely heavily on high-quality original projection data, limiting their ability to effectively restore undersampled or missing signals, and their practical application is limited by the difficulty in obtaining complete sinogram data. Iterative reconstruction methods (Chen et al., 2014) typically reconstruct images by iteratively optimizing an objective function. It usually alternates between forward and backward projections in the projection domain and the image domain until the objective function is minimized based on the convergence criterion. However, this method typically requires access to the raw data and bears a high computational cost. In addition, the quality of image reconstruction heavily relies on the precise setting of the objective function and hyperparameters. These limitations hinder the application of iterative reconstruction methods in clinical practice.

In contrast, image post-processing methods primarily address noise and artifacts within the image domain. Typical methods include non-local means filtering algorithm (Li et al., 2014), and block matching algorithm (Kang et al., 2013). Compared to the first two types of methods, post-processing has the advantage of not requiring original projection data from the CT vendor, making it easier to integrate into clinical CT imaging workflows.

In recent years, with the continuous improvement of computer performance, and the rapid development of cloud computing and distributed computing, deep learning-based image post-processing methods have achieved remarkable achievements in the field of LDCT denoising. Compared with traditional post-processing approaches, deep learning models are capable of automatically learning complex patterns in images, thereby exhibiting superior denoising performance. Currently, two popular network architectures, convolutional neural networks (CNNs) (LeCun et al., 1995) and Transformers (Vaswani, 2017), are widely applied in LDCT denoising. Furthermore, hybrid models combining these two architectures, along with other neural network frameworks, are continually being developed.

CNN-based methods effectively extract image features through convolutional layers, and have

achieved remarkable success in tasks such as image denoising (Kurmi et al., 2024; Kumar and Kurmi, 2022), object detection (Redmon, 2016), and image segmentation (Ronneberger et al., 2015). In recent years, CNNs have also been widely applied in medical image processing tasks, such as automated detection of knee joint synovial fluid in MR images (Iqbal et al., 2020), multi-class classification of skin lesions in dermoscopic images (Iqbal et al., 2021). In the field of LDCT denoising, several representative CNN-based models have likewise been proposed (Ming et al., 2020; Li et al., 2022; Gholizadeh-Ansari et al., 2020; Kyung et al., 2024; Meng et al., 2024; Zhang et al., 2024b; Ko et al., 2024). However, due to the limited receptive field of convolutional operators, CNNs exhibit certain limitations in modeling long-range dependencies and capturing global semantic information in images. Originally designed for natural language processing, Transformer has been successfully adapted to computer vision tasks, where its self-attention mechanism demonstrates remarkable capabilities in modeling long-range dependencies and capturing global semantic information in images (Li et al., 2025a). Vision Transformer was the first to apply this architecture to image classification, achieving performance comparable to CNNs and laying the foundation for the broader adoption of Transformers in visual tasks (Dosovitskiy et al., 2021). Swin Transformer improved computational efficiency by introducing a hierarchical architecture and shifted window attention, gradually evolving into a general-purpose backbone network for various vision tasks. However, Transformer-based models often incur high computational costs due to the quadratic complexity of the self-attention mechanism with respect to the number of input tokens. This characteristic presents a significant bottleneck in high-resolution image processing and edge computing scenarios.

Diffusion models have achieved remarkable results in visual tasks in recent years (Yang et al., 2023). Representative works, for example, the Denoising Diffusion Probabilistic Models (DDPM), proposed by Ho et al., define a forward process that gradually corrupts an image by adding Gaussian noise, and train a noise prediction network (typically a U-Net) to approximate the reverse denoising process, thereby progressively reconstructing a clean image from noise (Ho et al., 2020). On this basis, various extensions have been proposed to improve modeling efficiency. For instance, Denoising Diffusion Implicit Models (DDIM) accelerate the generation process by constructing a deterministic sampling path with non-Markovian properties (Song et al., 2021). Latent Diffusion Models (LDM) perform the diffusion process in a pretrained low-dimensional latent space, significantly reducing the computational burden for high-resolution image generation (Rombach et al., 2022). In the field of LDCT denoising, studies have demonstrated the effectiveness of diffusion models in suppressing noise artifacts and improving image quality (Xia et al., 2025; Ma et al., 2025). However, current diffusion models generally suffer from slow inference speed and high computational cost, which also limit their deployment in scenarios such as edge computing (Kebaili et al., 2025; Wang et al., 2024). To overcome these limitations, researchers are working to improve these models.

In this context, the structured state space sequence models (S4) have attracted extensive attention due to their efficient performance in long-range modeling (Gu et al., 2022). S4 optimizes its internal state representation and information transmission mechanism, significantly reducing computational and memory requirements, thus showing great potential in large-scale sequence modeling tasks. However, despite its breakthroughs in long-range modeling and computational efficiency, S4 still faces limitations in contextual reasoning and flexible information selection. To further enhance the model's performance in complex scenarios, the Mamba model (S6) is developed (Gu and Dao, 2024). Mamba integrates a selection mechanism into S4, allowing the model to selectively propagate or discard information along the sequence. This improvement boosts the model's contextual reasoning abilities while maintaining the computational efficiency of S4.

Currently, Mamba has been rapidly adopted in computer vision tasks. It unfolds image patches into sequences along the horizontal and vertical dimensions of the image, and performs bi-directional scanning along these two directions. This bidirectional scanning method enables VMamba to effectively capture both global and local information within images. At present, some studies have employed the network architectures based on visual Mamba (Zhao et al., 2024; Fu et al., 2025; Xie et al., 2024; Dang et al., 2024). Additionally, applications in LDCT image denoising have also been reported (Huang et al., 2024). However, the classic visual Mamba scanning method (row-column scanning) tends to disrupt the original spatial continuity between adjacent pixels near image boundaries, breaking the spatial adjacency relationships, which leads to local information loss and ultimately impairs the modeling of fine structures (Fu et al., 2024). This separation can undermine Mamba’s performance in visual tasks, particularly in medical imaging, where capturing fine structures and lesions is critical. To address this issue, we have improved the scanning method to ensure the spatial correlation between pixels in the image. Furthermore, by combining Mamba with CNN, we harness CNN’s strengths in local feature extraction along with Mamba’s global modeling capability, allowing the model to excel in handling the complex task of LDCT image denoising.

Current researches also ignore an important issue: the inability to quantitatively characterize noise distribution in predicted images. This may lead to problems such as excessive smoothing, misjudgment of lesions and key structures, and loss of spatial resolution. The Noise Power Spectrum (NPS) can quantitatively describe the noise texture in an image (Wilson et al., 2013). Therefore, this paper also utilizes NPS to guide deep learning LDCT denoising tasks, ensuring that the predicted images more accurately restore the noise distribution present in NDCT images, thereby improving overall image quality and diagnostic value.

The contributions of this study are summarized as follows:

1. We propose CT-Mamba, a hybrid convolutional state space model designed for LDCT image denoising. This model integrates the multi-scale analysis capability of wavelet transform, the powerful local feature extraction capacity of CNN, and the long-range dependency modeling strengths of Mamba, enabling comprehensive feature capture within the images.
2. We propose the Coherence Z-Scan State Space Block (CZSS), which introduces an innovative spatially coherent Z-shaped scanning scheme. This approach ensures spatial continuity between adjacent pixels in the image, enhancing the model’s ability to preserve details and improve denoising effectiveness.
3. To ensure that the denoised LDCT images can closely restore the noise texture of NDCT, this study also designs a Mamba-driven Deep NPS loss (Deep NPS loss).
4. Using radiomics, the proposed CT-Mamba was evaluated by comparing the statistical distribution of radiomics features in different organs between denoised LDCT images and NDCT images, as well as the mean absolute error of pairwise features.

## 2. Methodology

### 2.1. Preliminary: State Space Model

The state space model (SSM) is a mathematical description of a dynamic system which maps a one-dimensional input function or sequence  $x(t) \in \mathbb{R}^L$  to an output  $y(t) \in \mathbb{R}^L$  through hidden states  $h(t) \in \mathbb{R}^N$ . From a mathematical perspective, this process can be represented by a linear Ordinary Differential Equation (ODE):

$$\begin{aligned} h'(t) &= \mathbf{A}h(t) + \mathbf{B}x(t) \\ y(t) &= \mathbf{C}h(t), \end{aligned} \tag{1}$$

where  $\mathbf{A} \in \mathbb{R}^{N \times N}$  represents the state matrix, while  $\mathbf{B} \in \mathbb{R}^{N \times 1}$  and  $\mathbf{C} \in \mathbb{R}^{1 \times N}$  denote the projection parameters.

In order to integrate SSM into deep learning, the linear ordinary differential equation mentioned above needs to be discretized. Typically, the discretization of the SSM uses the Zero-Order Hold (ZOH) method. By incorporating a time scale parameter  $\Delta$ , the continuous parameters  $\mathbf{A}$  and  $\mathbf{B}$  are transformed into discrete parameters  $\bar{\mathbf{A}}$  and  $\bar{\mathbf{B}}$ , which can be defined as follows:

$$\begin{aligned}\bar{\mathbf{A}} &= \exp(\Delta\mathbf{A}) \\ \bar{\mathbf{B}} &= (\Delta\mathbf{A})^{-1}(\exp(\Delta\mathbf{A}) - I) \cdot \Delta\mathbf{B}\end{aligned}\quad (2)$$

After discretization, Equation (1) can be reformulated as:

$$\begin{aligned}h'(t) &= \bar{\mathbf{A}}h(t) + \bar{\mathbf{B}}x(t) \\ y(t) &= \mathbf{C}h(t)\end{aligned}\quad (3)$$

Equation (3) results in a discretized state space model that can be computed recursively. However, due to its sequential nature, this discretized recursive SSM is impractical for training. To enable efficient parallelized training, this recursive process can be reformulated as a convolution for computation:

$$\begin{aligned}\bar{\mathbf{K}} &= (\bar{\mathbf{C}}\mathbf{B}, \bar{\mathbf{C}}\bar{\mathbf{A}}\mathbf{B}, \dots, \bar{\mathbf{C}}\bar{\mathbf{A}}^{L-1}\bar{\mathbf{B}}) \\ y &= x * \bar{\mathbf{K}},\end{aligned}\quad (4)$$

where  $\bar{\mathbf{K}} \in \mathbb{R}^L$  represents a structured convolutional kernel,  $L$  denotes the length of the input sequence  $x$ , and  $*$  represents the convolution operation.

The recently proposed Mamba model makes further improvements by introducing a selective scanning mechanism. This allows parameters  $\mathbf{B}$ ,  $\mathbf{C}$  and  $\Delta$  to be dynamically adjusted based on the input  $x$  and contextual information. As a result, Mamba can model complex temporal dynamics more effectively, as the model can adapt to the evolving characteristics of the input data.

## 2.2. Framework Overview

In this paper, we propose CT-Mamba, a hybrid convolutional state space model designed for LDCT image denoising. This model integrates the multi-scale analysis capability of wavelet transform, the powerful local feature extraction ability of CNN, and Mamba’s long-range dependency modeling advantages, enabling it to comprehensively capture image features, as shown in Fig. 1(a).

In the initial stage of CT-Mamba, we designed a lightweight Progressive Feature Extraction Network (PFEN). This network extracts features at two levels, gradually capturing primary spatial features of LDCT images while incorporating raw information from LDCT images to provide richer spatial information for subsequent wavelet domain processing. Then, we applied a first-level wavelet transform to decompose the spatial information into a low-frequency component, a horizontal high-frequency component, a vertical high-frequency component, and a diagonal high-frequency component. This helps CT-Mamba better capture different frequency features in LDCT images. At the end of the network, we also designed a lightweight Progressive Feature Fusion Network (PFFN), which performs feature recombination across two branches. This enables efficient integration and refinement of features extracted from the wavelet domain. These two spatial networks work in tandem, effectively capturing and processing spatial information while significantly reducing the model’s computational complexity. Through combined processing in both the spatial and wavelet domains, the quality of the output image is notably enhanced.



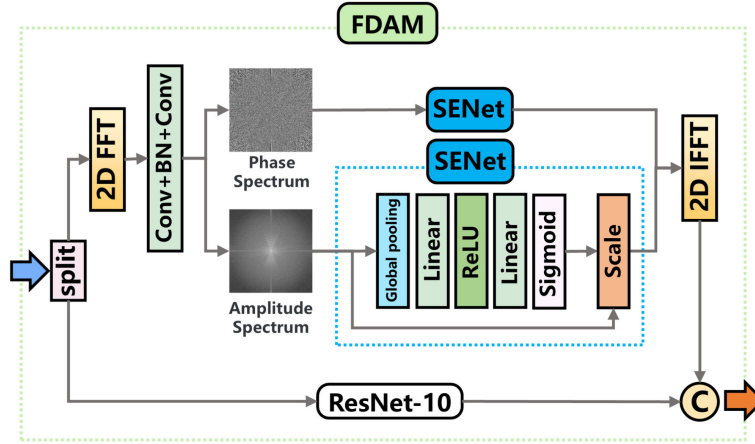


Figure 3: The structure of Frequency Domain Attention Module (FDAM).

of each frequency branch obtained by wavelet transform decomposition, as shown in Fig. 1(b). MSC-Mamba captures and fuses frequency features learned from three different scales ( $H \times W \times C$ ,  $\frac{H}{2} \times \frac{W}{2} \times 4C$ , and  $\frac{H}{4} \times \frac{W}{4} \times 16C$ ) by integrating Coherence Z-Scan State Space Block (CZSS). At lower scales, MSC-Mamba effectively captures global feature information, while at higher scales, it focuses more on local details. By combining feature learning across different scales, MSC-Mamba effectively ensures spatial coherence, providing superior denoising performance. Additionally, inspired by (Guo et al., 2023), we designed a Frequency Domain Attention Module (FDAM) based on Fourier transform to enhance the low-frequency features in the wavelet domain, as shown in Fig. 3. Each grid in the extracted Fourier spectrum contains global information on the low-frequency features, enabling efficient modeling of long-range spatial dependencies in the frequency domain. Enhanced by FDAM, richer low-frequency characteristics are provided for MSC-Mamba located in the low-frequency branch, thereby optimizing the modeling of overall structural information and improving CT-Mamba’s performance.

### 2.3. Coherence Z-Scan State Space Block

The Coherence Z-Scan State Space Block (CZSS) is a novel feature extraction unit specifically designed for tasks like medical imaging. Classic visual Mamba models, such as VMamba, which excel in natural image processing, utilize a row-column scanning order with bi-directional scanning in both horizontal and vertical directions. However, such scanning methods can overly separate some adjacent pixels when unfolding an image into a sequence. For instance, in horizontal scanning, there is a substantial distance between the end of one row and the beginning of the next, weakening spatial connections and subsequently hindering the capture of fine structures. To address this issue, inspired by the Zigzag scanning method in JPEG image compression theory, Z-SSM adopts a similar Z-shaped scanning approach to maintain spatial continuity between each adjacent pixel in the image, as shown in Fig. 4. Z-SSM employs multi-directional scanning and combined with a selective state space model SSM (S6) for modeling, ultimately merging the sequence and restoring it to a two-dimensional structure. This design ensures that subtle lesions and detailed information within the image are not overlooked, thereby enhancing the denoising effect of LDCT images.

A residual block with two convolutional layers is added to the front of CZSS can locally maintain the frequency-spatial correlation of input features and efficiently transfer local contextual information, thereby enabling more effective utilization and further optimization of these features, as represented by “Res” in Fig. 1(b). The CZSS begins by standardizing the input data through layer normalization,





algorithms.

In LDCT denoising tasks, neglecting the optimization of noise texture can severely impact the quality of denoised images. Therefore, quantitative analysis of the NPS is crucial for optimizing and evaluating image quality. In this study, we utilize NPS to guide the denoising of LDCT images for the first time, aiming to more accurately restore the noise texture in the denoised images. The NPS in this study is defined as follows:

$$\text{NPS}_{2D}(u, v) = \frac{p_x p_y}{N_x N_y} |\text{DFT}(\text{noise}(m, n))|^2, \quad (5)$$

where  $p_x$  and  $p_y$  represent the sampling intervals,  $N_x$  and  $N_y$  denote the two dimensions of the region of interest (ROI), and  $\text{noise}(m, n)$  is the noise image obtained by subtracting two images.  $(m, n)$  and  $(u, v)$  represent coordinates in the spatial and frequency domains, respectively.

Since it is difficult for medical images to separate noise from a single image, we designed a dual-branch structure optimized based on NPS, as shown in Fig. 5(a). By subtracting the NDCT image from the LDCT image, we obtain reference noise (denoted as  $\text{noise}_{\text{GT}}$ ,  $\text{noise}_{\text{GT}} = I_{\text{LDCT}} - I_{\text{NDCT}}$ ), and by subtracting the model-predicted image from the LDCT image, we obtain the predicted noise (denoted as  $\text{noise}_{\text{Pred}}$ ,  $\text{noise}_{\text{Pred}} = I_{\text{LDCT}} - I_{\text{Pred}}$ ). As each image can be abstracted as a combination of signal and noise, so the difference between these two noise components lies solely in the noise present in the model-predicted image versus the NDCT image. By analyzing NPS based on the pair of noise, we can guide the model to generate images with a noise distribution closer to that of NDCT images.

In the dual-branch structure, we designed an enhanced U-shaped network (u-Feature Net) to extract features from  $\text{noise}_{\text{GT}}$  and  $\text{noise}_{\text{Pred}}$ , as shown in Fig. 5(b). Low-frequency information is crucial in noise modeling, particularly for maintaining the stability of the overall noise structure and texture. Effective capture of low-frequency features is thus essential for improving noise texture. To address this, we designed a Mid and Low Frequency Feature Enhancement Connection (MLF-FEC) within u-Feature Net, specifically reinforcing the network’s processing of mid- and low-frequency information. Building on this, we applied an NPS transformation to the extracted noise features and incorporated the long-range modeling capability of CZSS to accurately capture the global noise feature distribution across the full frequency. This design effectively guides CT-Mamba in optimizing noise distribution.

After the full-band modeling of CZSS, the extracted  $\text{noise}_{\text{GT}}$  and  $\text{noise}_{\text{Pred}}$  features are converted into one-dimensional radial NPS (Radial NPS) to reduce complexity while retaining critical frequency information. The radialization principle is shown in Fig. 6. We then use L1 loss to measure the difference between the two radial NPS signals and design a correlation loss based on the Pearson correlation coefficient to guide model optimization. This approach ensures that the noise texture in the model’s denoised images more closely resembles that of NDCT images, thereby improving overall image quality and diagnostic value.

### 2.5. Overall Objective

The loss function measures the difference between the model’s predicted output (the denoised LDCT image) and the ground truth (NDCT image). While the model architecture determines the model’s complexity, the loss function controls how denoising characteristics are learned from the training dataset. To recover high-quality denoised CT images from LDCT, we combine different loss components into a hybrid objective function:

1) Pixel-level L1 Loss: Compared with L2 loss (mean square error, MSE), L1 loss does not overly penalize large errors between the predicted and NDCT images, so it can alleviate the blurriness and

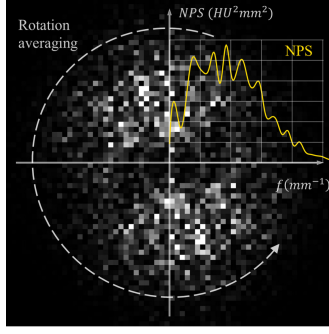


Figure 6: Schematic diagram of the radial transformation process of a 2D NPS signal.

unnatural effects caused by L2 loss to a certain extent. In our LDCT denoising task, it is defined as (6):

$$\mathcal{L}_{L1}(y, \hat{y}) = \left\| \hat{y} - y \right\|_1, \quad (6)$$

where  $\hat{y}$  represents the model's predicted output,  $y$  represents the ground truth NDCT image.

2) Deep NPS loss: This loss component ensures that the noise texture in the denoised image predicted by CT-Mamba is closer to that of the NDCT image. It is represented in conjunction with the description in Section 2.4 as (7):

$$\begin{aligned} \mathcal{L}_{\text{deep-NPS}}(x, y, \hat{y}) = & \gamma_1 \cdot \|\text{NPS}_{\text{radial}}(\phi(x, y) - \phi(x, \hat{y}))\|_1 \\ & + \gamma_2 \cdot (1 - \rho(\text{NPS}_{\text{radial}}(\phi(x, y)), \text{NPS}_{\text{radial}}(\phi(x, \hat{y})))) , \end{aligned} \quad (7)$$

where  $x$  represents the input LDCT image,  $\gamma_1$  and  $\gamma_2$  are weighting hyperparameters that respectively control the contributions of the L1 loss term and the correlation loss term.  $\phi(x, y)$  and  $\phi(x, \hat{y})$  represent the noise features extracted from the input image  $x$  and the real image  $y$ , and the input image  $x$  and the predicted image  $\hat{y}$  through a series of networks in each branch.  $\text{NPS}_{\text{radial}}(\cdot)$  represents the process of obtaining the radial NPS, and  $\rho(\cdot, \cdot)$  indicates the Pearson correlation coefficient, which measures the correlation between the two radial NPS, aiming to preserve the structural consistency of the noise texture.

3) Feature-Level Perceptual Loss: Perceptual loss captures information at the feature level using a pre-trained deep network. This loss is based on ResNet50 (He et al., 2016), pre-trained on the ImageNet dataset, with its weights frozen during training. Since the pre-trained ResNet50 accepts color images as input, we replicated the grayscale CT images across three channels to fit this input requirement. This approach has been validated in LDCT tasks (Yang et al., 2018). we extracted feature maps after its four main stages and used L2 loss to measure the similarity between the CT-Mamba output and the ground truth image. The perceptual loss is defined as (8):

$$\mathcal{L}_{\text{perceptual}}(y, \hat{y}) = \sum_{i=1}^4 \|f_i(y) - f_i(\hat{y})\|_2, \quad (8)$$

where  $f_i$  represents the feature map extracted at stage  $i$ ,  $y$  and  $\hat{y}$  denote the ground truth and predicted images, respectively.

In summary, the overall objective function is the weighted sum of each loss term (9):

$$\mathcal{L}_{\text{total}} = \lambda_1 \cdot \mathcal{L}_{\text{L1}} + \lambda_2 \cdot \mathcal{L}_{\text{deep-NPS}} + \lambda_3 \cdot \mathcal{L}_{\text{perceptual}}, \quad (9)$$

where  $\lambda_2 = (\gamma_1, \gamma_2)$ .

### 3. Experiment designs and results

#### 3.1. Datasets

In this work, we used a publicly released patient dataset for the 2016 NIH-AAPM-Mayo Clinic Low-Dose CT Grand Challenge (referred to as the Mayo dataset) (McCollough et al., 2017). This dataset contains paired low-dose and normal-dose abdominal images with a slice thickness of 1 mm for 10 patients. The quarter-dose LDCT images were generated by adding Poisson noise to the projection data of the NDCT images to mimic a noise level that corresponded to 25% of the full dose. To ensure the statistical robustness of our quantitative evaluations, we implemented a five-fold cross-validation strategy on the Mayo dataset. Specifically, the 10 patients were divided into 5 groups, with each fold using 2 patients as the test and the remaining 8 for training. For the visual analysis, we used data from 9 patients for model training, totaling 5,410 image pairs, while data from the remaining patient (L506) was used for testing model performance, totaling 526 pairs. Additionally, using the method in (Wang and Wang, 2022), we simulated paired low-dose and normal-dose images for 20 patients from the AMOS dataset (referred to as the Simulator dataset) for model training and validation (Ji et al., 2022). The low-dose images also correspond to a quarter of the normal dose. We used data from 19 patients for training, totaling 1,872 image pairs, and data from 1 patient (AMOS-0033) for testing model performance, totaling 106 pairs.

We also used in-house real low- and normal-dose head phantom data for experimental validation. Specifically, an anthropomorphic head phantom was scanned using a Cone-Beam Computed Tomography (CBCT) on-board imager (TrueBeam System, Varian Medical Systems, Palo Alto, CA). The phantom data comprises pairs of CT images acquired using low-dose parameters (80 kV, 100 mA) and normal-dose parameters (80 kV, 400 mA), with the low-dose settings representing one-quarter of the radiation exposure of the normal-dose configurations. The data directly reflect the noise and artifact characteristics under real low- and normal-dose conditions in daily CBCT for patient setup in image-guided radiotherapy.

#### 3.2. Implementation details

The proposed CT-Mamba model is implemented in PyTorch and trained in an environment equipped with an NVIDIA RTX 3090 Ti 24G GPU. The optimizer used is AdamW, with parameters set to  $(\beta_1, \beta_2) = (0.9, 0.999)$  and a weight decay of 0.02. The initial learning rate is set to  $1e-3$  and is gradually reduced to  $1e-6$  using cosine annealing. During training, each image is randomly cropped into four  $64 \times 64$  patches as input for each batch, with the batch size of 8. To balance the numerical relationship between the Deep NPS loss and the L1 loss and ensure training stability, the Deep NPS loss is not introduced during the first 10 epochs. Afterward, the hyperparameters of corresponding weights for the Deep NPS loss are set to  $\lambda_2 = (1e-4, 1e-2)$ . The perceptual loss weight  $\lambda_3$  is set to  $1e-2$ . The training process lasts for 250 epochs, with the final model selected based on the optimal loss achieved.

### 3.3. Experiment result and design

To demonstrate the effectiveness of the proposed CT-Mamba, we selected several advanced representative methods for comparative experiments, including RED-CNN (Chen et al., 2017), Uformer (Wang et al., 2022), CTformer (Wang et al., 2023), DDPM, and VM-UNet (Ruan and Xiang, 2024). RED-CNN is CNN-based methods, Uformer and CTformer are Transformer-based methods, DDPM is a diffusion model-based method, and VM-UNet is based on the Mamba framework.

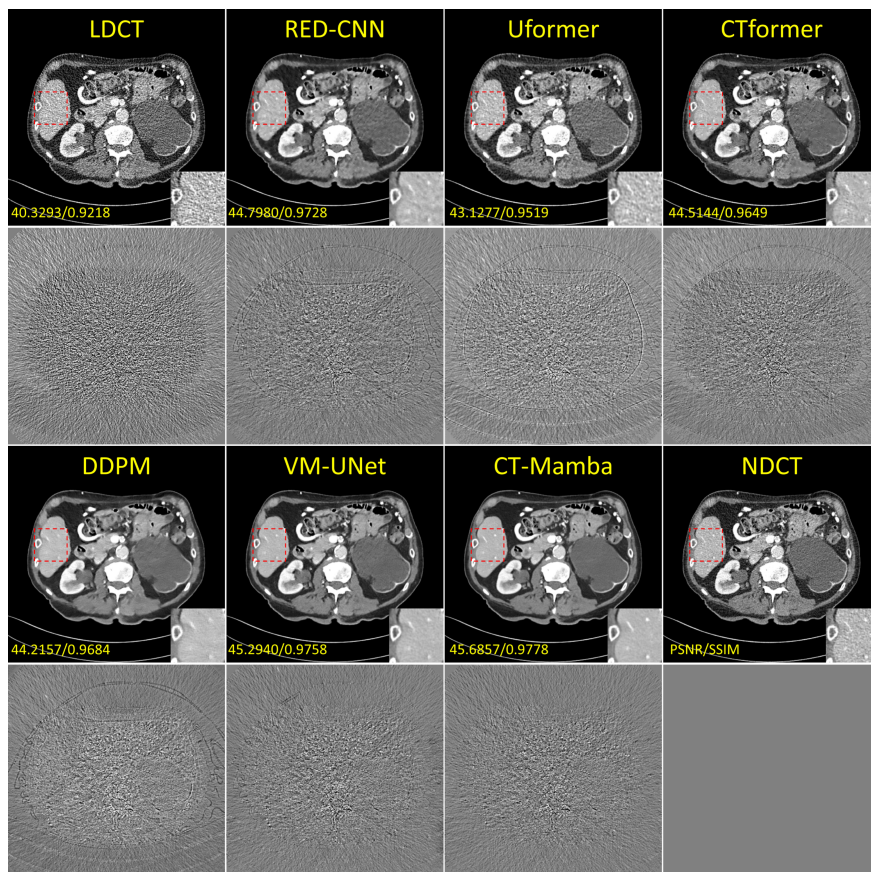


Figure 7: A set of slice prediction results and difference images obtained from the Mayo dataset L506 patient. The enlarged ROI (blood vessel) marked by the red dashed rectangle is located in the lower right corner of the image.

#### 3.3.1. Visual evaluation

This section presents the visual validation results of the CT-Mamba model compared to various baseline methods. In the Mayo dataset, we selected two representative slices, each containing the predicted results from each method along with their difference images relative to the NDCT images, to validate the comprehensive performance of our proposed method in LDCT processing, as shown in Fig. 7 and Fig. 8. To further assess detail representation, an enlarged view of the ROI which is marked by a red dashed rectangle is provided in the lower right corner of each image, along with the PSNR/SSIM quantitative results for each method displayed in the lower left corner. From the results shown in Fig. 7 and Fig. 8, all methods exhibit a certain degree of noise and artifact removal capability. However, compared to other methods, our proposed approach achieves the optimal processing performance, demonstrating excellent denoising competence in terms of detail preservation and artifact suppression. In the ROIs, we observe that CT-Mamba enhances the representation of fine structures

(such as blood vessels), as shown in Fig. 7; low-attenuation lesions are more clearly visible while maintaining well-defined tissue edges, as shown in Fig. 8.

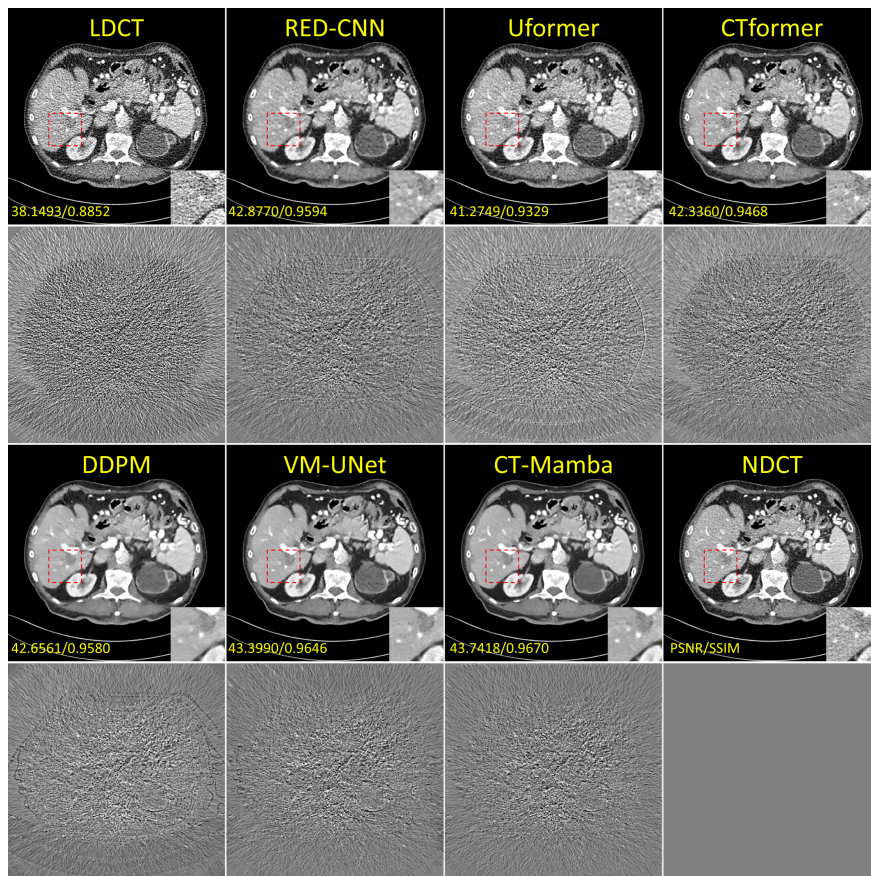


Figure 8: A set of slice prediction results and difference images obtained from the Mayo dataset L506 patient. The enlarged ROI (low-attenuation lesion, tissue edge) marked by the red dashed rectangle is located in the lower right corner of the image.

In Fig. 9, we also present the denoised results and difference images of a representative slice from the Simulator dataset, further validating the outstanding denoising performance and generalization capability of CT-Mamba across different datasets. The upper right corner of each predicted image shows the corresponding difference image. Additionally, we selected one representative case from the real dose head phantom data, as shown in Fig. 10. CT-Mamba effectively reduces noise while achieving the best perceptual quality, further demonstrating the generalizability of our method in clinical scenarios.

For the Mayo and Simulator datasets, we set the window level of the predicted results to 40 HU and the window width to 400 HU (i.e., a range from -160 HU to 240 HU). For the difference images, the window level is set to 0 HU with a window width of 200 HU (i.e., a range from -100 HU to 100 HU). For the real dose head phantom data, the window level was set to 0 HU and the window width to 800 HU (i.e., a range from -400 HU to 400 HU).

### 3.3.2. Quantitative analysis

Our method not only demonstrates significant optimization effects in subjective visual evaluation but also achieves excellent performance across multiple quantitative metrics. Most studies use common quantitative metrics in image processing to report their results, such as Peak Signal-to-Noise Ratio (PSNR), Structural Similarity Index Measure(SSIM), and Root Mean Square Error (RMSE). However,

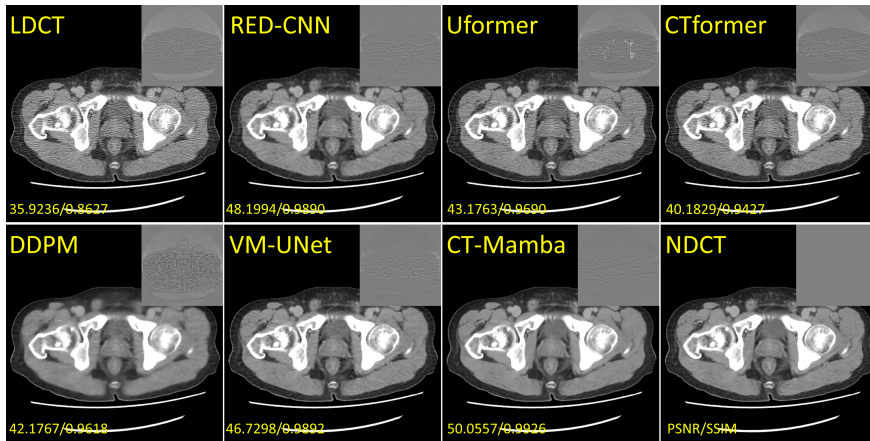


Figure 9: A set of slice prediction results and difference images obtained from the Simulator dataset AMOS-0033 patient, with the difference images located in the upper right corner.

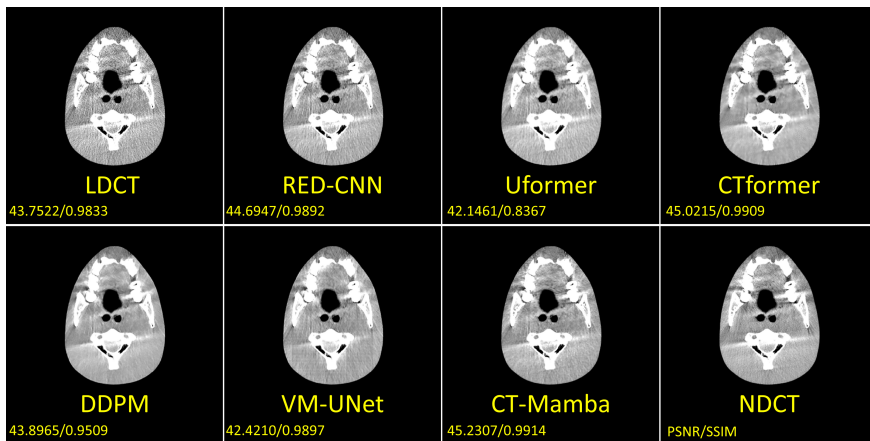


Figure 10: Visual comparison results on the real low- and normal-dose head phantom data, which comprises pairs of CT images acquired using on-board CBCT scanner with low-dose (80 kV, 100 mA) and normal-dose (80 kV, 400 mA) settings, respectively.

existing studies have indicated that these metrics do not sufficiently reflect clinical relevance (Patwari et al., 2023). Although human readers are considered as the gold standard for evaluating medical images, conducting multi-reader studies is time-consuming and costly. The research by Eulig et al. indicates that, compared to quantitative metrics like SSIM and PSNR for CT and MR images, various metrics including Visual Information Fidelity (VIF) have a higher correlation with human ratings (Eulig et al., 2024). Therefore, this study employs PSNR, SSIM, RMSE, and VIF for comprehensive evaluation. Additionally, in next section, we conducted a radiomics analysis to extract and compare the similarity of radiomic features.

In Table 1 and Table 2, we present the average quantitative results of PSNR, SSIM, RMSE, and VIF obtained from five-fold cross-validation on the Mayo dataset and from patient AMOS-0033 in the Simulator dataset, respectively. A comprehensive evaluation of the PSNR, SSIM, RMSE, and VIF metrics shows that CT-Mamba model outperforms the comparison methods across all quantitative metrics. Similarly, in Table 3, we present the average quantitative results of the real dose head phantom data. The results demonstrate that CT-Mamba maintains excellent performance under real-dose conditions, further demonstrating its potential for clinical application.

Table 1: Quantitative comparison of various methods on the Mayo dataset under five-fold cross-validation.

Method	PSNR $\uparrow$	SSIM $\uparrow$	RMSE $\downarrow$	VIF $\uparrow$
LDCT	40.8926 $\pm$ 0.8687	0.9309 $\pm$ 0.0113	37.8652 $\pm$ 3.7472	0.2709 $\pm$ 0.0150
RED-CNN	44.8327 $\pm$ 1.6669	0.9714 $\pm$ 0.0144	24.2221 $\pm$ 5.2109	0.3316 $\pm$ 0.0231
Uformer	46.1255 $\pm$ 0.7708	0.9802 $\pm$ 0.0032	20.5797 $\pm$ 1.8107	0.3557 $\pm$ 0.0167
CTformer	44.5024 $\pm$ 0.7586	0.9710 $\pm$ 0.0045	24.8519 $\pm$ 2.1773	0.3100 $\pm$ 0.0144
DDPM	42.8780 $\pm$ 1.2888	0.9533 $\pm$ 0.0143	29.8810 $\pm$ 4.7620	0.3020 $\pm$ 0.0151
VM-Unet	45.4553 $\pm$ 0.8614	0.9784 $\pm$ 0.0035	22.4240 $\pm$ 2.4696	0.3417 $\pm$ 0.0169
<b>CT-Mamba</b>	<b>46.2251<math>\pm</math>0.8006</b>	<b>0.9805<math>\pm</math>0.0033</b>	<b>20.3479<math>\pm</math>1.8592</b>	<b>0.3587<math>\pm</math>0.0180</b>

Table 2: The average quantitative results of different methods for patient (AMOS-0033) in the Simulator test dataset.

Method	PSNR $\uparrow$	SSIM $\uparrow$	RMSE $\downarrow$	VIF $\uparrow$
LDCT	38.7673	0.9099	35.5206	0.3573
RED-CNN	49.7609	0.9921	9.8209	0.5098
Uformer	44.9416	0.9795	17.1556	0.4241
CTformer	43.1905	0.9673	21.4047	0.4063
DDPM	43.7161	0.9696	19.7144	0.3776
VM-Unet	48.0132	0.9917	11.9833	0.4880
<b>CT-Mamba</b>	<b>51.2054</b>	<b>0.9942</b>	<b>8.2936</b>	<b>0.5444</b>

### 3.3.3. Radiomics reserach

Radiomics holds the potential to transform digital medical images into quantitative features that reveal underlying pathology, with promising applications in tumor classification and patient outcome prediction (Xia et al., 2023). In this study, the TotalSegmentator (Wasserthal et al., 2023) extension in 3D Slicer with a pretrained nnU-Net (Isensee et al., 2021) was utilized for automatic segmentation of target organs (aorta, right kidney, liver, stomach and small bowel), followed by manual adjustments to ensure accuracy. Under the five-fold cross-validation, for all patients in the Mayo dataset, 167 radiomics features (including 18 first-order features, 75 texture features and 74 wavelet-HHH features) were extracted from the volumes of each target organ using PyRadiomics (ver. 3.0). An ideal LDCT denoising algorithm is expected to produce denoised volumes with statistically similar radiomics features to those of NDCT volumes. The following two tests were designed to show statistical similarity:

(1) **Statistical Distribution of First-Order Features:** In statistical analysis, the Wilcoxon rank-sum test is commonly used to assess whether two datasets share the same distribution. For each volume, the Wilcoxon rank-sum test was employed to evaluate the consistency of radiomics features distribution between the denoised images and the reference NDCT ( $p > 0.05$ ). In Table 4, we show the p-values for each model across the target organs under five-fold cross-validation. A higher p-value indicates greater similarity to the radiomics features distribution of the NDCT. As shown in Table 4, while CTformer performed well for the liver and small bowel, its performance for the aorta and right kidney was poor, exhibiting significant deviations in radiomics features distributios compared to the NDCT and even underperforming compared to LDCT. In contrast, the proposed CT-Mamba demonstrated superior performance across multiple organs, including the aorta, right kidney, and stomach. Furthermore,

Table 3: The average PSNR, SSIM, RMSE, and VIF results of the real dose head phantom data.

Method	PSNR $\uparrow$	SSIM $\uparrow$	RMSE $\downarrow$	VIF $\uparrow$
LDCT	42.7276	0.9703	57.0131	0.2719
RED-CNN	44.0203	0.9809	48.9109	0.2880
Uformer	42.1097	0.8435	60.1177	0.2756
CTformer	44.6989	<b>0.9860</b>	45.1705	0.2862
DDPM	43.7502	0.9408	49.9756	0.2859
VM-Unet	44.0641	0.9857	48.3067	0.2847
<b>CT-Mamba</b>	<b>44.9698</b>	0.9859	<b>43.7079</b>	<b>0.2963</b>

Table 4: The p-values calculated using the Wilcoxon rank-sum test for each model under five-fold cross-validation. A p-value of under 0.05 indicates statistical difference. Pairs with statistical differences are marked by \*.

Method	Aorta	Right Kidney	Liver	Stomach	Small Bowel
LDCT	0.3922±0.2562	0.5373±0.3036	0.4044±0.1834	0.4767±0.2833	0.3959±0.2602
RED-CNN	0.4563±0.3196	0.4743±0.3285	0.5146±0.2938	0.5172±0.1997	0.7143±0.2599
Uformer	0.4376±0.3445	0.5783±0.2718	0.6046±0.1714	0.3047±0.2488	0.5771±0.2571
CTformer	0.3579±0.2883	0.4624±0.2734	<b>0.6815±0.1610</b>	0.5447±0.2712	<b>0.7263±0.2022</b>
DDPM	0.0002*±0.0003	0.0005*±0.0005	0.0001*±0.0001	0.0019*±0.0035	0.0009*±0.0014
VM-Unet	0.2805±0.3136	0.4487±0.3539	0.5497±0.2266	0.6527±0.2339	0.6527±0.2339
CT-Mamba	<b>0.4631±0.3179</b>	<b>0.6842±0.2898</b>	0.5722±0.2740	<b>0.6440±0.2634</b>	0.5417±0.2992

Table 5: The number of features with lower similarity ratios compared to LDCT (n/167, five-fold cross-validation).

Method	Aorta	Right Kidney	Liver	Stomach	Small Bowel
RED-CNN	42±26	48±32	45±27	68±30	51±29
Uformer	41±21	45±22	41±24	79±20	69±21
CTformer	<b>50±24</b>	<b>58±26</b>	45±7	67±27	61±12
DDPM	21±12	21±9	17±8	18±8	20±4
VM-Unet	47±23	48±23	45±22	74±13	59±14
CT-Mamba	43±23	43±19	<b>45±26</b>	<b>82±17</b>	<b>75±17</b>

its radiomics features distribution closely aligned with those of the NDCT for all other target organs. Notably, for the right kidney, the CT-Mamba outperformed all other models.

(2) **Pairwise Feature Similarity Ratio:** To quantitatively assess the similarity between the radiomics features of the target organs for all models and those of the NDCT, pairwise comparisons were performed for the all 167 radiomics features. The mean absolute error (MAE) between the features of each model and the corresponding NDCT features (10):

$$R_i = \left| \frac{V_{\text{NDCT}} - V_i}{V_{\text{NDCT}}} \right|, \quad (10)$$

where  $i$  was the different models, and  $V$  was the values of the selected radiomics features. A lower similarity ratio  $R_i$  indicates higher similarity between the features of the model and those of the NDCT. For each model, the  $R$  across the target organs were compared against  $R_{\text{LDCT}}$ , and the number of features with  $R_{\text{LDCT}}$  exceeding  $R$  was recorded.

As shown in Table 5, the proposed CT-Mamba demonstrated superior performance across all target organs. Notably, for the small bowel, where other models exhibited suboptimal performance, CT-Mamba achieved the best performance, further highlighting its robustness and effectiveness. The radiomics analysis indicate that the proposed CT-Mamba effectively preserves the shape and texture features of multiple organs within the LDCT images, demonstrating its potential value for clinical applications.

### 3.3.4. Ablation study

To evaluate the effectiveness of the core components of CT-Mamba, we designed three ablation experiments and conducted quantitative validation on patient L506 from the Mayo dataset. Each ablation model was trained using data from the remaining nine patients.

(A1) Effectiveness of Deep NPS loss: Excluding Deep NPS loss during training.

(A2) Effectiveness of the Scanning Method: Replacing the Coherence “Z” Scan with the following two methods: (A2.1) The classic row-column scanning strategy adopted by visual Mamba. (A2.2) The serpentine scanning strategy, which traverses alternating directions between adjacent rows or columns.

(M) Our complete model.

Fig. 11 presents the prediction results under three different scanning methods: (A2.1) row-column scanning, (A2.2) serpentine scanning, (M) the proposed Z-shaped scanning. The results demonstrate



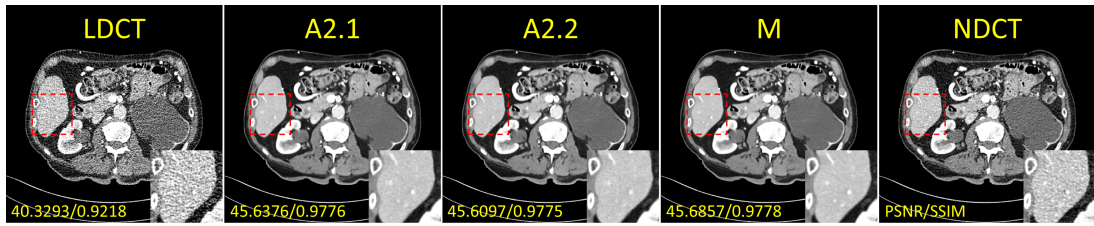


Figure 11: Comparison of prediction results under three scanning methods: (A2.1) row-column scanning, (A2.2) serpentine scanning, (M) the proposed Z-shaped scanning. The set range of the display window is a window level of 30 HU and a window width of 340 HU (i.e., a range from -140 HU to 200 HU).

Table 6: Quantitative comparison of different ablation experiments for patient (L506) in the Mayo test dataset.

Method	PSNR $\uparrow$	SSIM $\uparrow$	RMSE $\downarrow$	VIF $\uparrow$
LDCT	42.3509	0.9471	31.9809	0.2965
A1	47.0101	0.9830	18.5470	0.3679
A2.1	47.2245	0.9841	18.1040	0.3728
A2.2	47.1834	0.9840	18.1874	0.3711
<b>M</b>	<b>47.2825</b>	<b>0.9842</b>	<b>17.9850</b>	<b>0.3735</b>

that the Z-shaped scanning exhibits superior performance in structural modeling. In particular, it significantly enhances the clarity of vascular structures in the liver region, highlighting its advantages in maintaining spatial continuity and improving detail representation.

The quantitative results of each ablation experiment are summarized in Table. 6. The results indicate that the complete CT-Mamba model achieves the best performance across all metrics, further validating the significant contribution of each component to the overall performance of model.

To further investigate the impact of the Deep NPS loss on noise texture distribution in CT-Mamba, we conducted a radial NPS analysis on a uniform ROI with a size of  $32 \times 32$ , as marked in Fig. 12(a). The corresponding radial NPS of the ROI are shown in Fig. 12(b). By comparing the radial NPS of the ROI under conditions without (A1, orange curve) and with (M, green curve) the Deep NPS loss, the regulatory effect of this loss on noise can be more intuitively observed. The results indicate that the Deep NPS loss effectively guides the model to generate a noise distribution more consistent with that of NDCT. This is reflected in the radial NPS, where both the frequency distribution trend and amplitude response are closer to the ground truth (blue curve), with particularly significant improvements observed in the low-frequency range. This demonstrates that the Deep NPS loss effectively guides the network to produce noise textures more consistent with NDCT, validating its effectiveness in regulating noise structure.

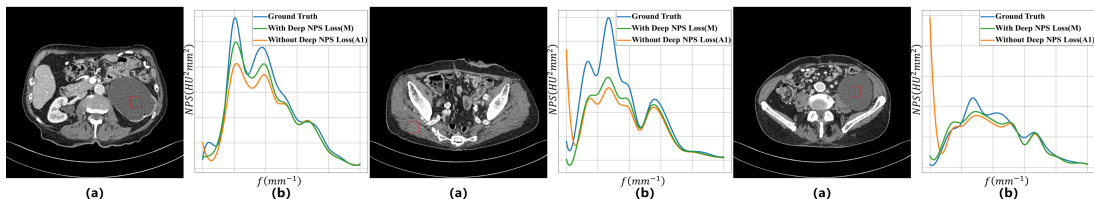


Figure 12: (a) Three representative CT slices from patient L506 in the Mayo dataset, with the red dashed box indicating the uniform ROI used for NPS analysis. (b) Radial NPS comparison of the corresponding ROIs: the green curve represents the complete model with Deep NPS loss (M), the orange curve represents the model without Deep NPS loss (A1), and the blue curve denotes the ground truth.

## 4. Conclusions

In this paper, we propose a hybrid convolutional state-space model, CT-Mamba, for LDCT image denoising. The model combines the multi-scale analysis capability of wavelet transform, the powerful local feature extraction ability of CNN and the long-range dependent modeling advantage of Mamba, so that it can fully capture the details and global information in LDCT images. We propose a new CZSS module, which adopts a spatially coherence “Z” Scan method, which effectively maintains the spatial continuity between adjacent pixels of the image, and further enhances the detail preservation and noise reduction capabilities of the model. Additionally, to the best of our knowledge, this is the first study to use NPS to guide deep learning in LDCT denoising tasks. We designed a deep NPS-loss driven by Mamba, aiming to ensure that the denoised image accurately restores the noise texture distribution of the NDCT image as much as possible, thereby improving the overall image quality and diagnostic value. We evaluated CT-Mamba on multiple datasets, and the experimental results show that our model performs excellently in denoising effectiveness, noise texture preservation, and radiomic feature restoration, showing potential to become a representative method of the Mamba framework for LDCT denoising tasks.

## CRedit authorship contribution statement

**Linxuan Li:** Writing - Original Draft, Methodology, Software, Conceptualization, Investigation.  
**Wenjia Wei:** Writing - Original Draft, Software, Methodology. **Luyao Yang:** Writing - Original Draft, Supervision, Validation. **Wenwen Zhang:** Visualization. **Jiashu Dong:** Data curation. **Yahua Liu:** Resources. **Hongshi Huang:** Resources. **Wei Zhao:** Writing – review and editing, Funding acquisition, Methodology, Conceptualization, Investigation, Supervision.

## Acknowledgments

This work was supported in part by the Natural Science Foundation of Zhejiang Province (No. LZ23A050002), Natural Science Foundation of Beijing (No. L246073), Natural Science Foundation of China (No. 12175012), the “111 center” (No. B20065), and the Fundamental Research Funds for the Central Universities, China.

## References

- Balda, M., Hornegger, J., Heismann, B., 2012. Ray contribution masks for structure adaptive sinogram filtering. *IEEE Trans. Med. Imaging* 31, 1228–1239.
- Bosch de Basea Gomez, M., Thierry-Chef, I., Harbron, R., Hauptmann, M., Byrnes, G., Bernier, M.O., Le Cornet, L., Dabin, J., Ferro, G., Istad, T.S., et al., 2023. Risk of hematological malignancies from ct radiation exposure in children, adolescents and young adults. *Nat. Med.* 29, 3111–3119.
- Chen, H., Zhang, Y., Kalra, M.K., Lin, F., Chen, Y., Liao, P., Zhou, J., Wang, G., 2017. Low-dose ct with a residual encoder-decoder convolutional neural network. *IEEE Trans. Med. Imaging* 36, 2524–2535.
- Chen, Y., Shi, L., Feng, Q., Yang, J., Shu, H., Luo, L., Coatrieux, J.L., Chen, W., 2014. Artifact suppressed dictionary learning for low-dose ct image processing. *IEEE Trans. Med. Imaging* 33, 2271–2292.

- Dang, T.D.Q., Nguyen, H.H., Tiulpin, A., 2024. Log-vmamba: Local-global vision mamba for medical image segmentation, in: *Proceedings of the Asian Conference on Computer Vision*, pp. 548–565.
- Dosovitskiy, A., Beyer, L., Kolesnikov, A., Weissenborn, D., Zhai, X., Unterthiner, T., Dehghani, M., Minderer, M., Heigold, G., Gelly, S., Uszkoreit, J., Houlsby, N., 2021. An image is worth 16x16 words: Transformers for image recognition at scale, in: *International Conference on Learning Representations*.
- Eulig, E., Ommer, B., Kachelrieß, M., 2024. Benchmarking deep learning-based low-dose ct image denoising algorithms. *Med. Phys.* .
- Fu, G., Xiong, F., Lu, J., Zhou, J., 2024. Ssumamba: Spatial-spectral selective state space model for hyperspectral image denoising. *IEEE Trans. Geosci. Remote Sens.* .
- Fu, L., Li, L., Lu, B., Guo, X., Shi, X., Tian, J., Hu, Z., 2025. Deep equilibrium unfolding learning for noise estimation and removal in optical molecular imaging. *Comput. Med. Imaging Graphics* 120, 102492.
- Gholizadeh-Ansari, M., Alirezaie, J., Babyn, P., 2020. Deep learning for low-dose ct denoising using perceptual loss and edge detection layer. *J DIGIT IMAGING* 33, 504–515.
- Gu, A., Dao, T., 2024. Mamba: Linear-time sequence modeling with selective state spaces. *First Conference on Language Modeling* .
- Gu, A., Goel, K., Ré, C., 2022. Efficiently modeling long sequences with structured state spaces. *The International Conference on Learning Representations (ICLR)* .
- Guo, S., Yong, H., Zhang, X., Ma, J., Zhang, L., 2023. Spatial-frequency attention for image denoising. *arXiv preprint arXiv:2302.13598* .
- He, K., Zhang, X., Ren, S., Sun, J., 2016. Deep residual learning for image recognition, in: *Proceedings of the IEEE conference on computer vision and pattern recognition*, pp. 770–778.
- Ho, J., Jain, A., Abbeel, P., 2020. Denoising diffusion probabilistic models. *Adv. Neural Inf. Process. Syst.* 33, 6840–6851.
- Huang, J., Zhong, A., Wei, Y., 2024. A new visual state space model for low-dose ct denoising. *Med. Phys.* .
- Iqbal, I., Shahzad, G., Rafiq, N., Mustafa, G., Ma, J., 2020. Deep learning-based automated detection of human knee joint’s synovial fluid from magnetic resonance images with transfer learning. *IET Image Process.* 14, 1990–1998.
- Iqbal, I., Younus, M., Walayat, K., Kakar, M.U., Ma, J., 2021. Automated multi-class classification of skin lesions through deep convolutional neural network with dermoscopic images. *Comput. Med. Imaging Graph.* 88, 101843.
- Isensee, F., Jaeger, P.F., Kohl, S.A., Petersen, J., Maier-Hein, K.H., 2021. nnu-net: a self-configuring method for deep learning-based biomedical image segmentation. *Nat. Methods* 18, 203–211.
- Ji, Y., Bai, H., Ge, C., Yang, J., Zhu, Y., Zhang, R., Li, Z., Zhanng, L., Ma, W., Wan, X., et al., 2022. Amos: A large-scale abdominal multi-organ benchmark for versatile medical image segmentation. *Advances in neural information processing systems* 35, 36722–36732.

- Kang, D., Slomka, P., Nakazato, R., Woo, J., Berman, D.S., Kuo, C.C.J., Dey, D., 2013. Image denoising of low-radiation dose coronary ct angiography by an adaptive block-matching 3d algorithm, in: *Medical Imaging 2013: Image Processing*, SPIE. pp. 671–676.
- Kebaili, A., Lapuyade-Lahorgue, J., Vera, P., Ruan, S., 2025. Multi-modal mri synthesis with conditional latent diffusion models for data augmentation in tumor segmentation. *Comput. Med. Imaging Graph.* 123, 102532.
- Ko, Y., Song, S., Baek, J., Shim, H., 2024. Adapting low-dose ct denoisers for texture preservation using zero-shot local noise-level matching. *Med. Phys.* 51, 4181–4200.
- Kumar, S., Kurmi, Y., 2022. Cnn-based denoising system for the image quality enhancement. *Multimed. Tools Appl.* 81, 20147–20174.
- Kurmi, Y., Viswanathan, M., Zu, Z., 2024. Enhancing snr in cest imaging: A deep learning approach with a denoising convolutional autoencoder. *Magn. Reson. Med.* 92, 2404–2419.
- Kyung, S., Won, J., Pak, S., Kim, S., Lee, S., Park, K., Hong, G.S., Kim, N., 2024. Generative adversarial network with robust discriminator through multi-task learning for low-dose ct denoising. *IEEE Trans. Med. Imaging* .
- LeCun, Y., Bengio, Y., et al., 1995. Convolutional networks for images, speech, and time series. *The handbook of brain theory and neural networks* 3361, 1995.
- Li, L., Wei, W., Lu, Y., Zhang, W., Zhang, Y., Zhao, W., 2025a. Bsonet: Deep learning solution for optimizing image quality of portable backscatter imaging systems. *IEEE Trans. Comput. Imaging* 11, 650–662.
- Li, L., Zhang, Z., Li, Y., Wang, Y., Zhao, W., 2025b. Ddoct: Morphology preserved dual-domain joint optimization for fast sparse-view low-dose ct imaging. *Med. Image Anal.* 101, 103420.
- Li, Q., Li, S., Li, R., Wu, W., Dong, Y., Zhao, J., Qiang, Y., Aftab, R., 2022. Low-dose computed tomography image reconstruction via a multistage convolutional neural network with autoencoder perceptual loss network. *QUANT IMAG MED SURG* 12, 1929.
- Li, Z., Yu, L., Trzasko, J.D., Lake, D.S., Blezek, D.J., Fletcher, J.G., McCollough, C.H., Manduca, A., 2014. Adaptive nonlocal means filtering based on local noise level for ct denoising. *Med. Phys.* 41, 011908.
- Ly, T., Xie, C., Zhang, Y., Liu, Y., Zhang, G., Qu, B., Zhao, W., Xu, S., 2024. A qualitative study of improving megavoltage computed tomography image quality and maintaining dose accuracy using cyclegan-based image synthesis. *Med. Phys.* 51, 394–406.
- Ma, X., Zou, M., Fang, X., Luo, G., Wang, W., Dong, S., Li, X., Wang, K., Dong, Q., Tian, Y., et al., 2025. Convergent–diffusion denoising model for multi-scenario ct image reconstruction. *Comput. Med. Imaging Graph.* 120, 102491.
- Manduca, A., Yu, L., Trzasko, J.D., Khaylova, N., Kofler, J.M., McCollough, C.M., Fletcher, J.G., 2009. Projection space denoising with bilateral filtering and ct noise modeling for dose reduction in ct. *Med. Phys.* 36, 4911–4919.

- McCollough, C.H., Bartley, A.C., Carter, R.E., Chen, B., Drees, T.A., Edwards, P., Holmes III, D.R., Huang, A.E., Khan, F., Leng, S., et al., 2017. Low-dose ct for the detection and classification of metastatic liver lesions: results of the 2016 low dose ct grand challenge. *Med. Phys.* 44, e339–e352.
- Meng, M., Wang, Y., Zhu, M., Tao, X., Mao, Z., Liao, J., Bian, Z., Zeng, D., Ma, J., 2024. Ddt-net: Dose-agnostic dual-task transfer network for simultaneous low-dose ct denoising and simulation. *IEEE J. Biomed. Health. Inf.* .
- Ming, J., Yi, B., Zhang, Y., Li, H., 2020. Low-dose ct image denoising using classification densely connected residual network. *KSII Trans. Internet Inf. Syst.* 14, 2480–2496.
- Patwari, M., Gutjahr, R., Marcus, R., Thali, Y., Calvarons, A.F., Raupach, R., Maier, A., 2023. Reducing the risk of hallucinations with interpretable deep learning models for low-dose ct denoising: comparative performance analysis. *Phys. Med. Biol.* 68, 19LT01.
- Redmon, J., 2016. You only look once: Unified, real-time object detection, in: *Proceedings of the IEEE conference on computer vision and pattern recognition.*
- Rombach, R., Blattmann, A., Lorenz, D., Esser, P., Ommer, B., 2022. High-resolution image synthesis with latent diffusion models, in: *Proceedings of the IEEE/CVF Conference on Computer Vision and Pattern Recognition (CVPR)*, pp. 10684–10695.
- Ronneberger, O., Fischer, P., Brox, T., 2015. U-net: Convolutional networks for biomedical image segmentation, in: *Medical image computing and computer-assisted intervention–MICCAI 2015: 18th international conference, Munich, Germany, October 5-9, 2015, proceedings, part III 18*, Springer. pp. 234–241.
- Ruan, J., Xiang, S., 2024. Vm-unet: Vision mamba unet for medical image segmentation. *arXiv preprint arXiv:2402.02491* .
- Song, J., Meng, C., Ermon, S., 2021. Denoising diffusion implicit models, in: *Int. Conf. Learn. Represent.*
- Vaswani, A., 2017. Attention is all you need. *Advances in Neural Information Processing Systems* .
- Wang, D., Fan, F., Wu, Z., Liu, R., Wang, F., Yu, H., 2023. Ctformer: convolution-free token2token dilated vision transformer for low-dose ct denoising. *Phys. Med. Biol.* 68, 065012.
- Wang, J., Li, T., Lu, H., Liang, Z., 2006. Penalized weighted least-squares approach to sinogram noise reduction and image reconstruction for low-dose x-ray computed tomography. *IEEE Trans. Med. Imaging* 25, 1272–1283.
- Wang, S., Wang, A.S., 2022. Simulating arbitrary dose levels and independent noise image pairs from a single ct scan, in: *7th International Conference on Image Formation in X-Ray Computed Tomography*, SPIE. pp. 460–466.
- Wang, T., Xia, W., Lu, J., Zhang, Y., 2024. A review of deep learning ct reconstruction from incomplete projection data. *IEEE Trans. Radiat. Plasma Med. Sci.* 8, 138–152.
- Wang, Z., Cun, X., Bao, J., Zhou, W., Liu, J., Li, H., 2022. Uformer: A general u-shaped transformer for image restoration, in: *Proceedings of the IEEE/CVF conference on computer vision and pattern recognition*, pp. 17683–17693.

- Wasserthal, J., Breit, H.C., Meyer, M.T., Pradella, M., Hinck, D., Sauter, A.W., Heye, T., Boll, D.T., Cyriac, J., Yang, S., et al., 2023. Totalsegmentator: robust segmentation of 104 anatomic structures in ct images. *Radiology-Artificial Intelligence* 5.
- Wilson, J.M., Christianson, O.I., Richard, S., Samei, E., 2013. A methodology for image quality evaluation of advanced ct systems. *Med. Phys.* 40, 031908.
- Xia, J., Yan, M., Yang, X., Zhang, X., Tao, Z., 2025. Cmc-diffusion: Curve matching correction diffusion model for Idct denoising. *Biomed. Signal Process. Control* 103, 107333.
- Xia, T.y., Zhou, Z.h., Meng, X.p., Zha, J.h., Yu, Q., Wang, W.l., Song, Y., Wang, Y.c., Tang, T.y., Xu, J., et al., 2023. Predicting microvascular invasion in hepatocellular carcinoma using ct-based radiomics model. *RADIOLOGY* 307, e222729.
- Xie, H., Zhang, H., Chen, Z., Tan, T., 2024. Precision dose prediction for breast cancer patients undergoing imrt: The swin-umamba-channel model. *Comput. Med. Imaging Graphics* 116, 102409.
- Yang, L., Zhang, Z., Song, Y., Hong, S., Xu, R., Zhao, Y., Zhang, W., Cui, B., Yang, M.H., 2023. Diffusion models: A comprehensive survey of methods and applications. *ACM Comput. Surv.* 56, 1–39.
- Yang, Q., Yan, P., Zhang, Y., Yu, H., Shi, Y., Mou, X., Kalra, M.K., Zhang, Y., Sun, L., Wang, G., 2018. Low-dose ct image denoising using a generative adversarial network with wasserstein distance and perceptual loss. *IEEE Trans. Med. Imaging* 37, 1348–1357.
- Zhang, J., Gong, W., Ye, L., Wang, F., Shangguan, Z., Cheng, Y., 2024a. A review of deep learning methods for denoising of medical low-dose ct images. *Comput. Biol. Med.* , 108112.
- Zhang, W., Lyu, T., Li, Y., Chen, Y., Sun, B., Zhao, W., 2025. Data-driven contrast-enhanced dual-energy ct imaging via physically constrained attention. *IEEE Trans. Radiat. Plasma Med. Sci.* .
- Zhang, Y., Wan, Z., Wang, D., Meng, J., Ma, F., Guo, Y., Liu, J., Li, G., Liu, Y., 2024b. Multi-scale feature aggregation and fusion network with self-supervised multi-level perceptual loss for textures preserving low-dose ct denoising. *Phys. Med. Biol.* 69, 105003.
- Zhang, Z., Liang, X., Zhao, W., Xing, L., 2021. Noise2context: context-assisted learning 3d thin-layer for low-dose ct. *Med. Phys.* 48, 5794–5803.
- Zhao, S., Chen, H., Zhang, X., Xiao, P., Bai, L., Ouyang, W., 2024. Rs-mamba for large remote sensing image dense prediction. *IEEE Trans. Geosci. Remote Sens.* .